JOURNAL OF CATALYSIS **164,** 194–206 (1996)
ARTICLE NO. 0375

Adsorbed Species and Reaction Rates for NO–CO over Rh(111)

H. Permana,* K. Y. Simon Ng,* Charles H. F. Peden,† Steven J. Schmieg,‡ David K. Lambert,‡ and David N. Belton‡,[1]

*Wayne State University, Department of Chemical Engineering, Detroit, Michigan 48202; †Environmental Molecular Sciences Laboratory, Pacific Northwest National Laboratory,[2] Richland, Washington 99352; and ‡Physics and Physical Chemistry Department, General Motors Research and Development Center, Warren, Michigan 48090-9055

Received February 8, 1996; revised June 20, 1996; accepted June 21, 1996

We have studied the reaction of NO with CO over a Rh(111) catalyst by monitoring the infrared (IR) intensity of surface CO and NO at various partial pressures of NO (P_{NO}), CO (P_{CO}), and sample temperatures (T). Reaction rates for the products (CO_2, N_2O, and N_2) were previously measured at the same conditions in our apparatus [*J. Phys. Chem.* 99, 16344 (1995)]. Surface coverages were observed both at $P_{NO} = 8$ Torr, where the reaction yields mostly N_2O and the selectivity is insensitive to either P_{CO} (1 to 40 Torr) or T (<673 K), and at $P_{NO} = 0.8$ Torr, where the major product changes from N_2O below 635 K to N_2 above 635 K. Changes in the surface coverages of NO and CO correlate well with the observed changes in N_2O selectivity. Below 635 K, where N_2O formation is favored, NO dominates the surface. Above 635 K, where N_2 formation is preferred, CO is the majority surface species. Our IR data support a model in which product N_2O and N_2 are formed as adsorbed N reacts with either adsorbed NO or N, respectively. In an additional kinetic experiment, we used isotopically labeled N_2O to show that gas phase N_2O is not an intermediate to N_2 formation at 648 K—this helps to rule out an alternative model. In our IR experiments, two types of spectra were obtained with a Fourier transform IR spectrometer. Polarization spectra were obtained using two fixed polarizers, one before the sample, oriented to pass approximately equal amounts of *s*- and *p*-polarized light, and one after the sample that selected *s*- or *p*-polarized light. Spectra obtained with *s*- and *p*-polarized light were ratioed. We also obtained conventional reflectance absorbance IR spectra. In a separate calibration experiment with NO on Rh(111) in ultrahigh vacuum we observed five IR bands at 1448, 1530, 1590, 1643, and 1693 cm^{-1}. We attribute all of these to bridging NO, most likely at threefold hollow sites. As NO coverage increases up to saturation, the distribution of population among these bands (and their individual frequencies) gradually changes—the average vibrational frequency of the NO increases from ~1440 to ~1650 cm^{-1}. From the linear dependence of the integrated IR absorption on NO coverage we find that the vibrational polarizability of the adsorbed NO is 0.20 ± 0.02 $Å^3$, a factor 6.5 larger than for free NO. This increase, proportionally larger than for CO on transition metal surfaces, is explained by the facile charge transfer that accompanies donor–acceptor bonding between NO and Rh(111).

I. INTRODUCTION

Automobile catalytic converters react CO and nitrogen oxides (NOx) over Rh containing catalyst particles (1). New government regulations require that vehicles emit less NOx, CO, and hydrocarbons (2). A vehicle's NOx emission rate is determined by the ability of NO to compete with O_2 to supply the oxygen atoms that oxidize CO to CO_2. As a result, vehicle NOx emissions are affected by the kinetics of the NO–CO reaction over Rh.

In this paper we use IR spectroscopy to study the CO–NO reaction at the Rh(111) surface. We have previously shown that this has similar kinetics to the CO–NO reaction over practical Rh/Al_2O_3 catalysts (3) and have studied it at the elementary step level (3–7). In particular, the NO–CO reaction over Rh and Pt–Rh single crystals gives the same three products (CO_2, N_2O, and N_2) as it does over supported Rh and Pt–Rh catalysts (3–10). Of the several proposed NO–CO reaction mechanisms (8–16), we favor (3, 5, 6) the simplest:

$$CO(g) + S \Leftrightarrow CO(ad), \quad [1]$$

$$NO(g) + S \Leftrightarrow NO(ad), \quad [2]$$

$$NO(ad) + S \Rightarrow N(ad) + O(ad), \quad [3]$$

$$CO(ad) + O(ad) \Rightarrow CO_2(g) + 2S, \quad [4]$$

$$NO(ad) + N(ad) \Rightarrow N_2O(g) + 2S, \quad [5]$$

$$N(ad) + N(ad) \Rightarrow N_2(g) + 2S. \quad [6]$$

This explains kinetic data for NO pressure (P_{NO}) > 1 Torr (133.3 N m^{-2}); however, uncertainty in the rate constants for steps [3] and [5] has left other possible explanations open. In the above model, the rate expressions for steps [5]

[1] To whom correspondence should be addressed. Fax: (810) 986-3901. E-mail: dbelton@cmsa.gmr.com.

[2] Pacific Northwest National Laboratory is a multiprogram National Laboratory operated for the U.S. Department of Energy by Batelle Memorial Institute under Contract DE-AC06-76RLO 1830.

0021-9517/96 $18.00

and [6] are

$$R_{\text{form}}^{N_2O} = \theta_N \theta_{NO} \nu \exp\left[\frac{-E_a}{RT}\right], \quad [7]$$

$$R_{\text{form}}^{N_2} = \theta_N^2 \nu \exp\left[\frac{-(E_a - \alpha_N \theta_N)}{RT}\right]. \quad [8]$$

Here, θ_{NO} and θ_N are the coverages of NO and N, respectively, ν is the preexponential factor, E_a is the activation energy, and α_N is N atom coverage dependence of E_a. For the conditions where N_2O selectivity is insensitive to both T and P_{NO} our model predicts that steps [5] and [6] have similar E_a and that θ_{NO} and θ_N remain roughly constant. Further, for conditions where N_2O selectivity is sensitive to T or P_{NO}, the model implies that θ_{NO} changes. We use IR spectroscopy to monitor θ_{NO}.

In this paper we also use isotopically labeled N_2O to determine the contribution of gas phase N_2O to N_2 formation. This helps to distinguish between proposed NO–CO reaction mechanisms.

II. EXPERIMENTAL

The experiments were performed in a moderate pressure (<100 Torr) reactor coupled to an ultrahigh vacuum (UHV) analysis chamber. The reactor was equipped with a gas chromatograph (GC) and a Fourier transform IR spectrometer. Details of the reactor system, gas handling methods, sample preparation and cleaning, and GC measurements have been reported previously (3–7, 17). New to the system for this paper is a Fourier transform IR spectrometer (Mattson RS-10000 with a water cooled source). The optical system used in our experiment is shown in Fig. 1. The spectra we show are averages of 1000 scans taken at 4 cm^{-1} resolution. (This took 2.5 min.) The entire beam path to the detector was purged with dry CO_2-free air. The IR beam was focused onto the sample with an off-axis parabola (25.4 cm focal length). The light entered and exited the reactor through ZnSe windows. Before entering the reactor, the light passed through a wire-grid polarizer (on a ZnSe substrate). This polarizer was oriented to pass approximately equal intensities of *s*- and *p*-polarized light. (The electric field of *s*-polarized light is parallel to the sample surface; *s*- and *p*-polarized light are orthogonal). The IR beam's angle-of-incidence to the sample was $86 \pm 3^\circ$. (The range is due to the beam's circular diameter at the focusing mirror. A visible He–Ne laser beam, concentric with the IR beam, was used to align the IR beam and measure the angel-of-incidence.) After the IR beam exited the reactor, it passed through a second wire-grid polarizer that was oriented to pass either *s*- or *p*-polarized light. Finally, an off-axis parabola focused the light onto a liquid N_2 cooled HgCdTe detector that responded to optical frequencies above 750 cm^{-1}.

Figure 2 shows the calculated IR response versus angel-of-incidence for an adsorbate on Rh. The calculation is for

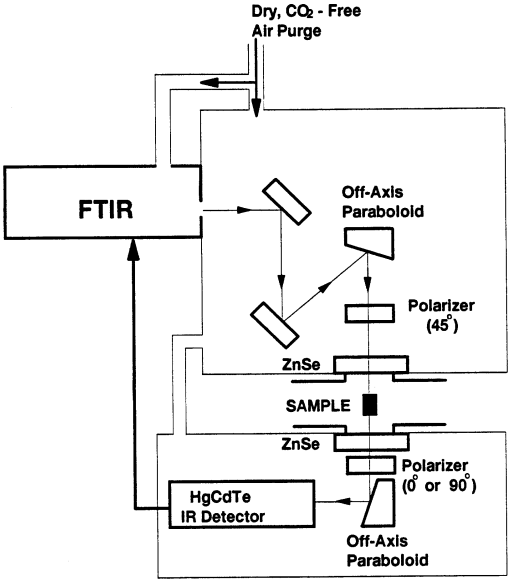

FIG. 1. Optical system used for RAIRS measurements of the adsorbed surface species on Rh(111) during NO–CO reaction.

p-polarized light and an adsorbate (like CO or NO) that vibrates along the surface normal. The IR response of such an adsorbate to *s*-polarized light is zero; moreover, even a randomly oriented adsorbate has negligible response to *s*-polarized light. The measured optical properties of Rh

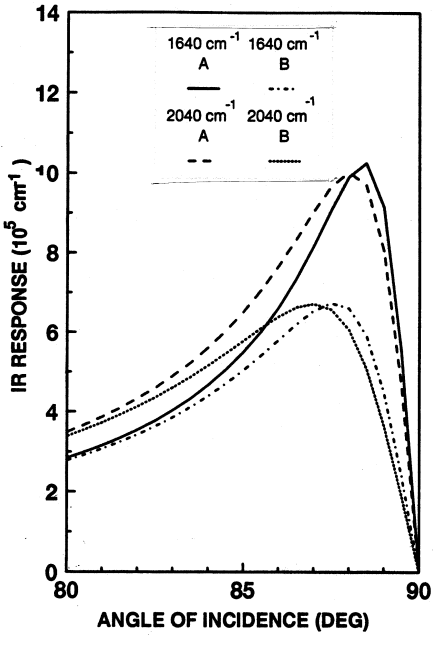

FIG. 2. IR response β versus angle-of-incidence of the light, calculated for an adsorbate on Rh. The light is *p*-polarized. Curves labeled A and B use Rh's optical properties from Refs. (18) and (19), respectively. The two optical frequencies, 1640 and 2040 cm^{-1}, are those of NO and CO, respectively.

(18, 19) at the NO and CO vibrational frequencies, 1640 and 2040 cm^{-1}, respectively, have been used for the calculation (20, 21). Since there have been two measurements of Rh's optical properties, and these do not agree, calculations with each are shown. In the experiment, the incident light's angular range includes each curve's peak response.

The IR response plotted in Fig. 2 relates the measured $A = \int(\Delta R/R)\, d\nu$ to the local properties of the adsorbate. Here $(\Delta R/R)$ is the adsorbate induced change in reflectivity R, normalized by R of the clear surface, and ν is the optical frequency in cm^{-1}. For a collection of uncoupled Lorentzian oscillators on a surface, with density N_s per unit area, resonant frequency ν_0, and vibrational polarizability α_v,

$$A = N_s \alpha_v \nu_0 (\pi/2)\beta, \qquad [9]$$

where β is the quantitiy plotted in Fig. 2. β is evaluated for the imaginary part of the adsorbate's susceptibility as in Appendix A of Ref. (20). In the (incorrect) approximation that the metal is perfectly reflecting, a different expression that relates A to α_v has been given by Chabal (22). The difference between these two approaches has been discussed by Tobin (21).

Two methods were used to obtain absorbance spectra: polarization spectroscopy (PS) and conventional RAIRS. The first, PS, makes use of the difference between an adsorbate's interaction with *s*- and *p*-polarized light. (Gas molecules interact identically with *s*- and *p*-polarized light.) Two spectra are measured sequentially: one with *s*-polarized light and the other with *p*-polarized light. Their ratio shows only adsorbed sepcies, without spectral interference from gas species. This is important in the present experiment since there are four gas phase species (NO, CO, CO_2, and N_2O) that interfere with the adsorbed species.

We found that PS worked well from 1800 to 2200 cm^{-1}. The polarizer before the sample was needed to eliminate PS artifacts—probably because the light from the spectrometer was partially polarized. However, even with the polarizer, we still observed irreproducible features near the vibrational frequency of bridging NO (about 1600 cm^{-1}) with intensities of about 10^{-3} absorbance units. These were especially troublesome since the NO stretch mode is of similar intensity. In subsequent experiments we have traced these artifacts in the PS sepctra to an IR absorbing film on the ZnSe windows we were using. The artifacts disappeared when the ZnSe windows were replaced by CaF_2 windows.

Conventional RAIRS, in which a spectrum with NO on the surface is ratioed to a spectrum of the clean surface, was used to avoid the spectral artifacts near 1600 cm^{-1} in the present experiments. Even though both the gas phase and adsorbed species are seen with RAIRS, the vibrational frequency of adsorbed NO (near 1600 cm^{-1}) discriminated it from gas phase NO and N_2O. For the reference spectra the pressure was 10^{-8} Torr. To avoid RAIRS artifacts, we found that sample T had to be the same for both the sample and reference spectra. However, others have reported that for their system, T during the reference spectrum did not affect the quality of their RAIRS data (23).

The spectra reported here are split into two regions. For 1800 to 2200 cm^{-1} we use PS. This range includes the region for atop and bridging CO and atop NO. For 1200 to 1800 cm^{-1}, conventional RAIRS allows us to see bridging NO.

The reaction conditions used to obtain our IR spectra were chosen to allow comparison with previous kinetic data for the same sample in the same apparatus (3). However, some of the kinetic measurements described in Ref. (3) ($P_{NO} = 8$ Torr) were obtained with the reactor operated in batch mode while all of the IR spectra reported here were collected with the reactor operated in flow mode. Rates measured in flow mode during the present experiment agreed to within 25% with the rates previously measured in batch mode.

III. RESULTS

3.1. Kinetic Data

Since our IR measurements are made under the same reaction conditions, we first summarize our previously published kinetic data (3). Figure 3 shows the measured turnover number (TON) in molecules/site · sec for the three

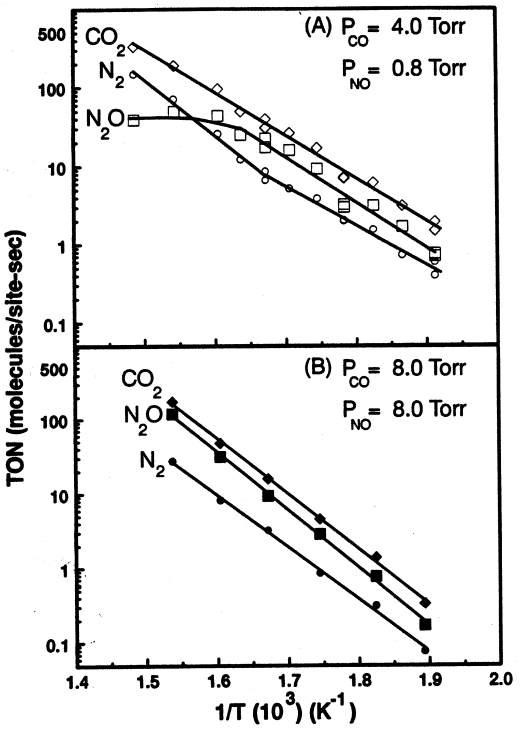

FIG. 3. Specific rates of CO_2, N_2O, and N_2 formation for the NO–CO reaction over Rh(111) as a function of $(1/T)$ using: (A) $P_{NO} = 0.8$ Torr and $P_{CO} = 4$ Torr and (B) $P_{NO} = P_{CO} = 8$ Torr.

products: CO_2, N_2O, and N_2. Data are given for $P_{CO} = 4$ Torr, $P_{NO} = 0.8$ Torr, and $P_{CO} = P_{NO} = 8$ Torr. The NO conversion was always below 15%. The low T limit, 523 K, was set by the need for enough NO conversion to accurately measure the products. The high T limit, 673 K, was set by thermal instability. The rate of this exothermic reaction increases with T until the heat released cannot be compensated by our temperature controller. The apparent activation energies and frequency factors are given in Table 1 of Ref. (3).

The selectivity of the reaction for N_2O formation is defined as

$$S_{N_2O} = \frac{\text{moles } N_2O}{\text{moles } N_2O + \text{moles } N_2}. \qquad [10]$$

Figure 4 shows S_{N_2O} as a function of T for the same conditions as in Fig. 3. The data in Fig. 4 extend to higher T since we could still meausre the relative rates of N_2 and N_2O formation even when the reaction rate was too fast to measure TONs.

The effect of CO pressure (P_{CO}) on the TONs of CO_2, N_2O, and N_2 is shown in Fig. 5. Two values of P_{NO} were used: 0.8 and 8 Torr. At $P_{NO} = 0.8$ Torr, the formation rates for the three products are zero order in P_{CO} up to ~4 Torr; −0.3 order at higher P_{CO}. At $P_{NO} = 8$ Torr, the reaction rate of each of the three products was zero order in P_{CO} over the entire range.

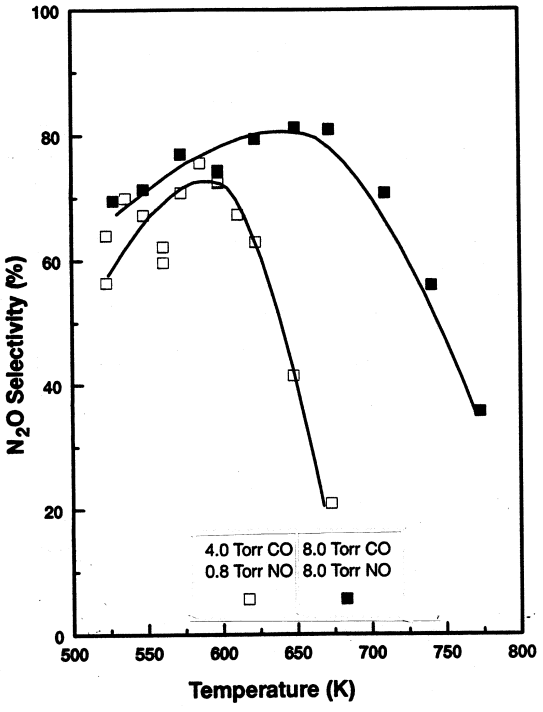

FIG. 4. Selectivity for N_2O as a function of T using two different reactant mixtures. The open symbols are for 4 Torr CO/0.8 Torr NO and the closed symbols are for 8 Torr CO/8 Torr NO.

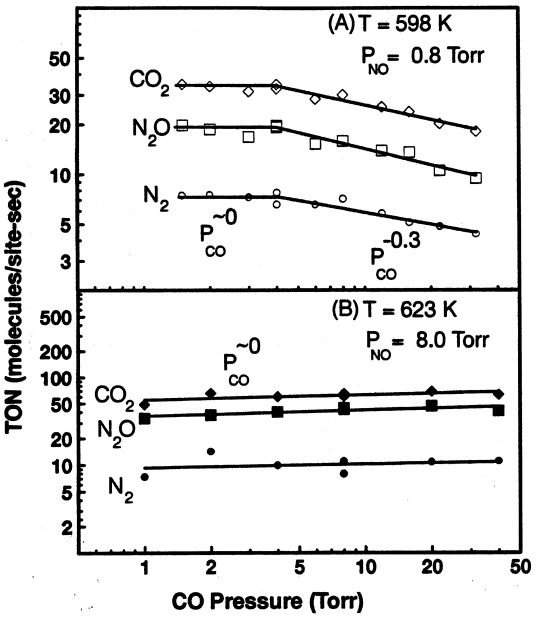

FIG. 5. Effect of CO pressure on the specific rates for CO_2, N_2O, and N_2 formation for the NO–CO reaction over Rh(111) using: (A) 0.8 Torr NO and (B) 8 Torr NO.

The effect of P_{NO} on the TONs for CO_2, N_2O, and N_2 is shown in Fig. 6. Two values of P_{CO} were used: 4 and 8 Torr. At $P_{CO} = 4$ Torr, the TONs for CO_2 and N_2O are zero order only for $P_{NO} > 0.8$ Torr; the rates for CO_2, N_2O, and N_2 formation are half, first, and zero order, respectively for P_{NO} between 0.4 and 0.8 Torr. At $P_{CO} = 8$ Torr, the

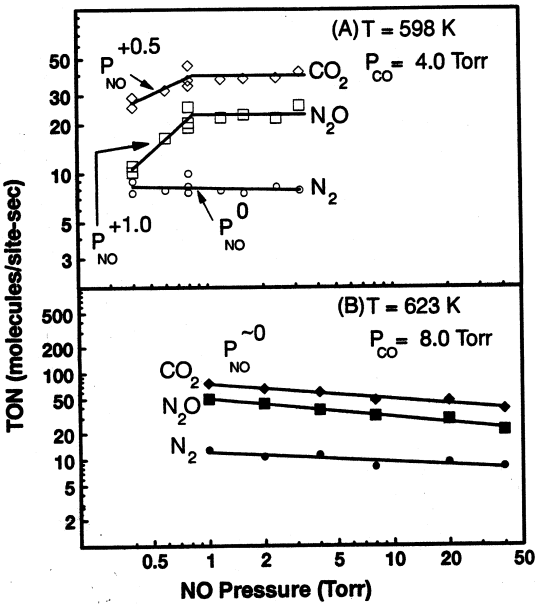

FIG. 6. Effect of NO pressure on the specific rates for CO_2, N_2O, and N_2 formation for the NO–CO reaction over Rh(111) using two different reaction conditions: (A) 4 Torr CO and (B) 8 Torr CO.

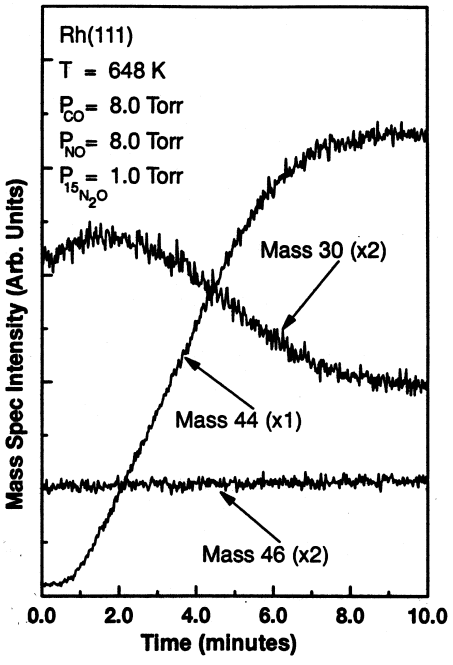

FIG. 7. Mass spectrometer intensity versus time for the reaction of 8 Torr ^{14}NO, 8 Torr ^{12}CO, and 1 Torr $^{15}N_2O$. The reaction was carried out in a batch mode with the initial T at 25 K. After ~1.5 min. T was ramped at 15 K/s up to 648 K, where it was kept constant.

reaction rate of each of the three products was zero order in P_{NO} over the entire range.

Figure 7 presents the results of an experiment with isotopically labeled $^{15}N_2O$ mixed in the gas phase with ^{14}NO and ^{12}CO. We wanted to determine whether readsorption of gas phase N_2O is an important step for N_2 formation in the NO–CO reaction. This experiment was run in a batch mode. A leak valve passed the reactants and products to the ionizer of a mass spectrometer in the UHV system. The experiment started with 8 Torr of ^{14}NO, 8 Torr of ^{12}CO and 1 Toor of $^{15}N_2O$ mixed in the reactor and with the sample at room temperature. Next the leak valve was opened and the mass spectrometer signals for masses 44 ($^{12}CO_2$ and $^{14}N_2O$), 30 (^{14}NO), 28 (^{12}CO and $^{14}N_2$), and 46 ($^{15}N_2O$) were allowed to stabilize. Adsorption of NO on the UHV chamber walls caused the NO signal to drift initially. However, mass 46 and 44 stabilized after ~5 min. The mass spectrometer data shown in Fig. 7 begin then. At ~1 min, T began to be ramped at 15 K/s up to 648 K. At ~1.5 min, T reached 648 K; it was held fixed for the remainder of the experiment. As can be seen in Fig. 7, for times >1 min, mass 44 (^{12}CO and $^{14}N_2O$) increased linearly and mass 30 (^{14}NO) decreased linearly with time for ~5 min. After ~7 min all the signals had stabilized; the reaction had stopped. Based on the reactor pressure data we estimate >95% conversion. No change occurred in the mass 46 signal ($^{15}N_2O$); therefore, none of the gas phase $^{15}N_2O$ was consumed. This shows that readsorption of gas phase N_2O is not an important step in the reaction mechanism in this temperature range. In a second experiment we showed that gas phase N_2O is consumed only after 100% conversion of the NO and only if the reaction temperature is raised more than 50 K. After complete NO conversion at these elevated temperatures, the $CO + N_2O$ reaction runs as we have previously reported (4).

3.2. RAIRS Measurements under Reaction Conditions

As discussed in Section II, two different methods were used to obtain IR spectra of the adsorbed species: PS for 1800–2200 cm^{-1} and conventional RAIRS for 1200–1800 cm^{-1}.

The 1200–1800 cm^{-1} spectra are shown in Fig. 8. Two reaction conditions were used: one with 4 Torr CO and 0.8 Torr NO, the other with 8 Torr CO and 8 Torr NO. For both, IR spectra were obtained for eight values of T from 523 to 673 K. The doublet at 1274 and 1302 cm^{-1} is from gas phase N_2O (a product of the reaction). Because the reaction runs faster at higher T, the N_2O bands grow as T is increased. The sloping background above 1730 cm^{-1} is from gas phase NO (one of the reactants). The only surface feature in Fig. 8, near 1640 cm^{-1}, is due to adsorbed NO. As is discussed in the Appendix, the most recent experiments suggest that this NO is at threefold hollow sites. Under reaction conditions, the full width at half maximum of the NO feature is approximately 100 cm^{-1}, larger than

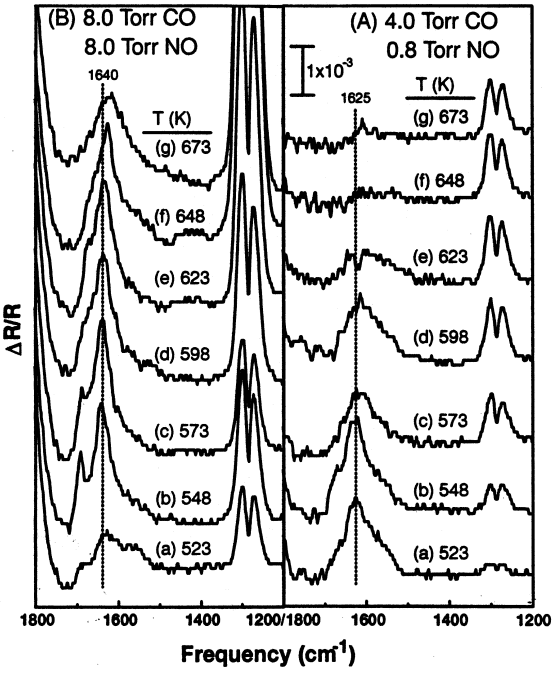

FIG. 8. NO stretching region of the IR spectrum from the NO–CO reaction over Rh(111) as a function of T. The data were obtained using two different reactant mixtures: (A) $P_{NO} = 0.8$ Torr and $P_{CO} = 4$ Torr and (B) $P_{NO} = P_{CO} = 8$ Torr. The adsorbed NO is seen in the range 1625 to 1640 cm^{-1}.

the 25 to 60 cm^{-1} width of the bands from adsorbed NO on this surface in UHV (Fig. 13). The spectra taken under reaction conditions with low T and high P_{NO} also show extra structure in the bridging NO band.

The 1800–2200 cm^{-1} spectra obtained with PS are shown in Fig. 9. These were acquired at the same time as those in Fig. 8. The actual spectra extend to 4000 cm^{-1} but since no surface species were detected above 2100 cm^{-1} they are not presented here. [Isocyanate was observed on Rh(111) at ~2200 cm^{-1} in separate experiments, but it is below our detection limit under all the conditions we report here.] As discussed in Section II, PS sees only surface species. The 1800 to 2200 cm^{-1} range includes the vibrational frequencies of atop and bridge CO as well as atop NO. We have observed all of these in separate experiments at 273 K, but for the NO–CO reaction conditions used here, we detect only atop CO (2030–2050 cm^{-1}) and never any atop NO or bridge CO.

In Fig. 10 we plot the integrated IR intensities A_{NO} and A_{CO} of bridge NO and atop CO, respectively, as functions of $1/T$. (This facilitates comparison with the kinetic data shown in Fig. 3.) The IR data can be compared directly with the kinetic data since the experimental conditions were the same. With 4 Torr CO and 0.8 Torr NO, A_{NO} (defined as the integrated area under all the NO peaks) decreases from 0.19 to 0.05 cm^{-1} as T increases from 548 to 673 K; over the same range, A_{CO} is constant at 0.04 cm^{-1} up to 573 K,

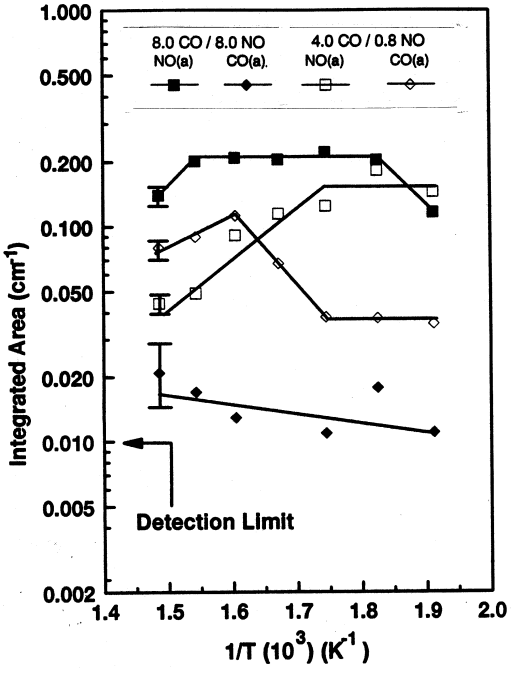

FIG. 10. Integrated intensities of surface NO and CO peaks from Figs. 8 and 9 as a function of $(1/T)$. The open symbols are for 4 Torr CO/0.8 Torr NO and the closed symbols are for 8 Torr CO/8 Torr NO.

increases sharply to 0.11 cm^{-1} as T increases to 623 K, and then decrease back to 0.08 cm^{-1} at 673 K. With 8 Torr CO and 8 Torr NO, A_{NO} is constant at about 0.20 cm^{-1} over most of the T range, while A_{CO} remains small at about 0.015 cm^{-1}, only slightly above our detection limit.

In Fig. 11 we present A_{NO} and A_{CO} versus P_{CO}. The data were taken in exactly the same manner as the T dependent data in Figs. 8–10. The spectra of adsorbed NO and adsorbed CO are similar to those shown in Fig. 8; therefore, only the integrated areas are reported. Two values of P_{NO} were used, 0.8 and 8 Torr, both with $T = 598$ K. With P_{NO} fixed at 0.8 Torr, A_{NO} decreased by a factor of 2.2 as P_{CO} increased from 1.5 to 32 Torr. Simultaneously, A_{CO} increased by about a factor of 4. With P_{NO} fixed at 8 Torr, A_{NO} remained roughly constant as P_{CO} is increased from 1.6 to 32 Torr; however, A_{CO} increased smoothly above about 6 Torr CO. At $P_{CO} < 6$ Torr, A_{CO} was below our detection limit.

A similar comparison of integrated IR intensity versus P_{NO} is shown in Fig. 12 for $P_{CO} = 4$ and 8 Torr, both at 598 K. Again, the same NO and CO features are seen that were observed in Fig. 8. The IR data is almost identical at the two CO pressures. At the lowest P_{NO} (0.4 Torr), A_{NO} was only 0.02 cm^{-1}, which is barely above our detection limit. As P_{NO} increased, A_{NO} increased linearly (the line in Fig. 12 is 0.9 order in P_{NO}) before leveling off between 2 and 3 Torr of NO. For higher NO pressures, A_{NO} was roughly constant. As for A_{CO}, as P_{NO} increased from 0.4 to 40 Torr, A_{CO} fell from 0.12 cm^{-1} to our detection limit by $P_{NO} = 3.2$ Torr.

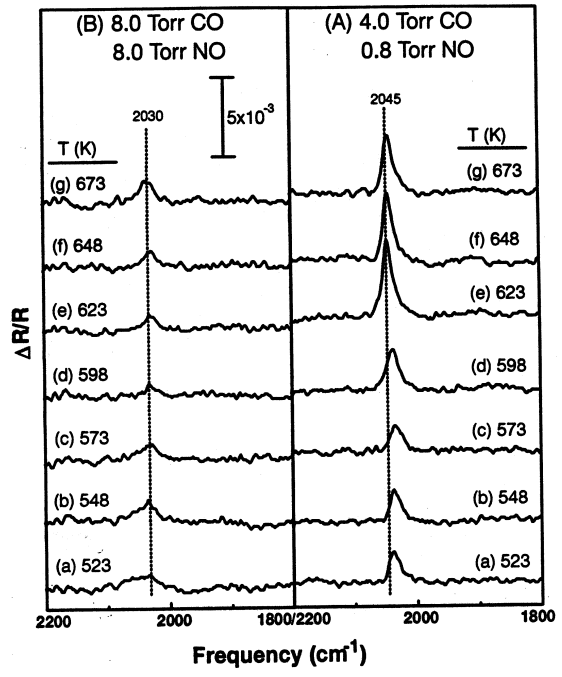

FIG. 9. IR spectrum of the adsorbed CO as a function of T from the NO–CO reaction over Rh(111) using two different reaction conditions: (A) $P_{NO} = 0.8$ Torr and $P_{CO} = 4$ Torr and (B) $P_{NO} = P_{CO} = 8$ Torr. Surface CO is seen at 2030 to 2045 cm^{-1}.

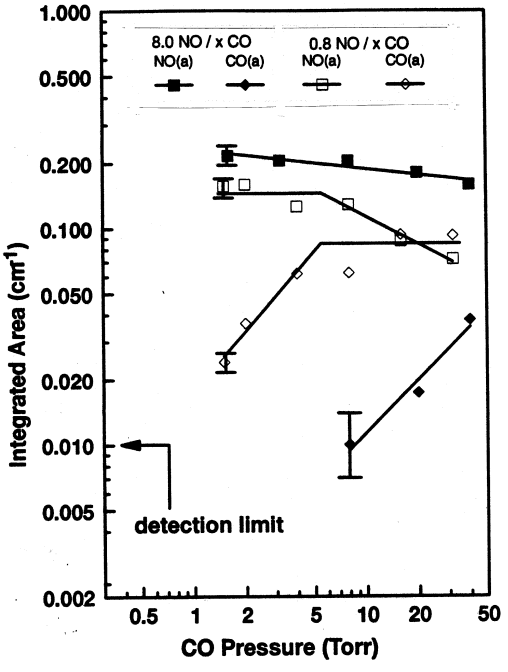

FIG. 11. Integrated intensities for the CO and NO peaks as a function of CO pressure at 598 K using two different NO pressures: 0.8 and 8 Torr.

3.3. Dependence of RAIRS Intensity on Surface Coverage

In order to use measured A to estimate surface coverage one must first perform a calibration experiment. In Figs. 13 and 14 we present the data used to correlate A_{NO} and θ_{NO}. With only NO on the surface, XPS was used to measure θ_{NO}.

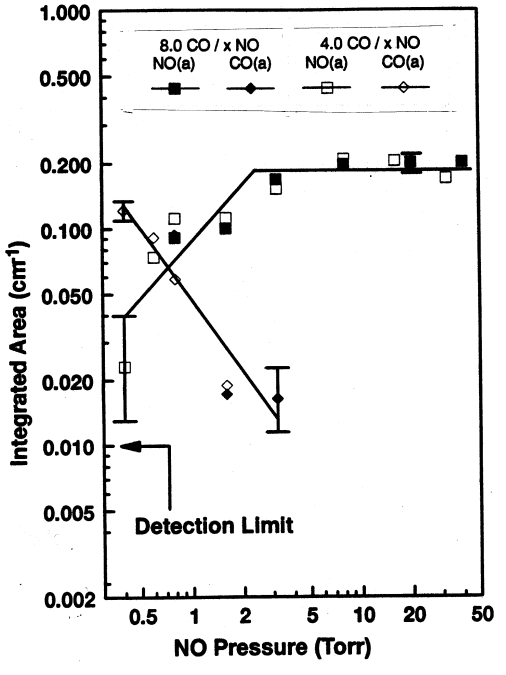

FIG. 12. Effect of NO pressure on the adsorbed NO and CO and 598 K using 8 and 4 Torr of CO.

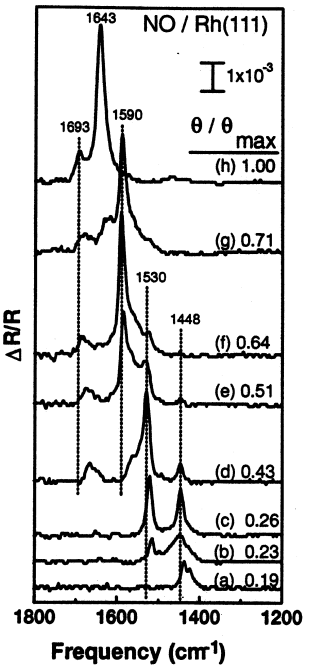

FIG. 13. IR spectra of adsorbed NO on Rh(111) in UHV at various NO coverages. Coverage is given relative to saturation and was determined using XPS. Adsorption and measurement were performed at 200 K.

In these figures, coverage is given as θ/θ_{max}, where θ_{max} is the maximum amount of NO that can be adsorbed in a UHV experiment. For NO on Rh(111), $\theta_{max} = 0.75$ ML or 1.2×10^{15} cm^{-2} (24). Figure 13 shows the NO stretching region for different initial NO coverages, dosed under UHV conditions using a directed NO doser and background pressures in the 8×10^{-10} Torr range. During dosing, the sample was cooled to 200 K (with liquid N_2) to prevent NO dissociation. After dosing with NO, XPS data were obtained and then the IR spectrum was measured. Figure 13 shows five resolved NO stretching bands. As θ_{NO} increase, ν_{NO} of the individual bands increases. Intensity also gradually shifts from the low ν_{NO} to the high ν_{NO} bands with increasing θ_{NO}. Note that the frequency of a given peak is determined by the total θ_{NO} and not just by the coverage of a particular species—as the peaks at 1448 and 1530 cm^{-1} decline in intensity they do not shift back to lower frequency. Above 70% of saturation three peaks are observed that have approximately the same frequencies as the three peaks observed under reaction conditions. Thus it is likely that they are the same species.

In Fig. 14 we present the A_{NO} versus θ_{NO} measured by XPS. The line in the plot is a linear regression through the eight lowest coverage points (<0.7 ML) and gives an indication of our detection limit (0.05 ML). There is good linearity between A_{NO} and θ_{NO} up to 70% of saturation or ~0.5 ML. This linearity is remarkable with four different IR peaks. Presumably the modes all have similar cross sections. Thus, we can accurately relate θ_{NO} to A_{NO} provided

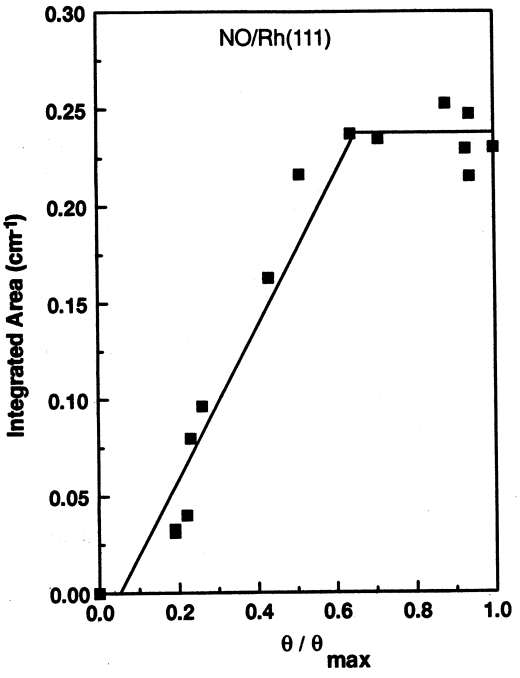

FIG. 14. Total integrated IR intensity as a function of NO coverage on Rh(111) in UHV. Coverage is given relative to saturation and was determined using XPS. Adsorption and measurement were performed at 200 K.

that $\theta_{NO} < 0.5$ ML. Since A_{NO} does not decline at $\theta_{NO} > 0.5$ ML (as sometimes occurs with CO), we do not risk confusing $\theta_{NO} < 0.5$ ML with θ_{NO} between 0.5 and 0.75 ML. The cluster of data points at high θ_{NO} gives an estimate of the precision of measured A_{NO} (± 0.02 cm^{-1}).

The slope of A_{NO} as a function of N_s in Fig. 14 together with the known values of β and ν_0 in Eq. [9] give the vibrational polarizability α_v of NO on Rh(111): 0.20 ± 0.02 Å^3. [If our data are analyzed with the expression Chabal (22) derived for a perfectly reflecting substrate, $\alpha_v = 0.0173$ Å^3.] For comparison, free NO oriented in the direction of the applied electric field has (20, 25) $\alpha_v = 0.031$ Å^3; free CO similarly oriented has (20, 25) $\alpha_v = 0.050$ Å^3; and CO on Cu(100) (26), Ru(100) (26), and Pt(111) (27) have $\alpha_v = 0.27$, 0.28, and 0.22 Å^3, respectively. The ratio of α_v for free NO and CO (0.62) is comparable to the ratio between NO on Rh(111) and CO and Cu(100) (0.74), Ru(100) (0.71), and Pt(111) (0.91). We did not measure α_v for CO on Rh(111) but we would expect it to fall within this range. On Pd(111) and Pd(100), the IR cross sections of NO and CO are also found to be approximately equal (28, 29).

The factor 6.5 increase in α_v for NO on Rh(111) relative to free NO is larger than the fractional increase for CO on Cu(100) (5.4), Ru(100) (5.6), and Pt(111) (4.4). However, an even larger increase in α_v to 0.40 ± 0.02 Å^3 (a factor 8.0 increase) has been reported for CO on an evaporated film of Au (30). The increase of α_v for CO on Cu(100) relative to free CO has been explained (31) as a consequence of the donor-acceptor bonding between the CO and the metal, which allows facile exchange of charge between them. Since the bonding of NO to Rh(111) is similar to the bonding of CO to transition metal surfaces—the main difference is that NO can either donate or accept charge since the π orbital that is empty for free CO contains one electron for free NO—a similar increase in α_v is also expected. The difference in α_v between free NO and NO on Rh(111) also includes any screening of the local field at the NO by electrons from the metal.

IV. DISCUSSION

4.1. Interpretation of the RAIRS Data

We rely upon RAIRS data as an indicator of NO and CO surface coverages. For CO on metal surfaces it is frequently found that A_{CO} is a linear function of θ_{CO} only at low coverage. At high θ_{CO} the slope of A_{CO} as a function of θ_{CO} decreases with increasing θ_{CO} and can flatten out or even become negative—the relationship is no longer monotonic. Examples include CO on Cu(111) (32), Cu(100) (33), Ru(100) (34), Pd(100) (35), and Rh(100) (36). [However, in an electrochemical experiment (37) with CO on Rh(111) in water, A_{CO} as a function of θ_{CO} was linear up to the saturation θ_{CO}.] In the standard model (26), saturation of the A_{CO} as a function of θ_{CO} is ascribed to screening of the local IR electric field by the electronic polarizability α_e of the nearby CO. To fit (26) the data of A_{CO} as a function of θ_{CO} for CO on Cu(100), the model uses $\alpha_e = 3$ Å^3. With the field directed along the molecular axis, α_e of free CO and NO (36) are similar, 2.33 ± 0.01 and 2.30 ± 0.01 Å^3, respectively. Consequently, the standard model would not suggest that the form of A as a function of θ for NO and CO should be qualitatively different. The abrupt saturation of A_{NO} as a function of θ_{NO} in Fig. 14 is actually consistent with data for CO on Pd(100) (35) but not with the standard model. Recent experiments (39–41) with CO on Pt have also obtained data of A_{CO} versus θ_{CO} that clearly contradict the standard model so this is not surprising. We accept the data in Figs. 13 and 14 which show that A_{NO} is a linear function of θ_{NO} up to about 0.5 ML. At larger θ_{NO}, A_{NO} saturates, but it does not decrease.

For both NO and CO on Rh(111) it has been established that the saturation coverage yields a (2×2) LEED pattern at 0.75 ML (24, 42, 43). In our experiment the NO and CO molecules are well mixed on the surface. This follows from previous UHV studies of mixed NO and CO overlayers on a Rh(111) surface (44, 45). In these two papers, Root *et al.* used HREELS to show that NO and CO can form either segregated or well mixed layers. Segregation tends to occur upon low temperature adsorption (<200 K). Island formation is indicated when coadsorption of NO with a low concentration of surface CO causes both linear and bridging CO bands to appear (typical of local CO coverage

near saturation). In our data we never see any bridging CO. This shows that the NO and CO layers are well mixed.

4.2. Comparison of IR Data to the NO–CO Reaction Model

One objective of this study was to use IR data obtained under reaction conditions to test models of the NO–CO reaction. We discuss the data at $P_{NO} > 1$ Torr first. The kinetic data in Figs. 3–6 show that the N_2O selectivity is insensitive to T, P_{CO}, and P_{NO} in a wide range: 500 K $\leq T \leq$ 700 K, 1 Torr $\leq P_{CO} \leq$ 40 Torr, and 1 Torr $\leq P_{NO} \leq$ 40 Torr. The model described in Section I explains these observations. Most of the rate constants for the elementary steps in the model have been measured under UHV conditions. The model predicts that NO dissociation is the rate limiting step. θ_{NO} is quite high, and θ_{CO} is very low under the reaction conditions given above.

Figures 8–12 show the RAIRS data. Consider first the effect of reaction conditions on θ_{CO} with $P_{NO} > 1$ Torr and 500 K $< T <$ 700 K. The RAIRS measurements show that θ_{CO} is near our detection limit: $\theta_{NO} \approx 0.02$ ML. This is best seen by examining Figs. 9B and 10 (effect of T), Fig. 11 (effect of P_{CO}), and Fig. 12 (effect of P_{NO}). In only one data set (Fig. 11, closed diamonds) does A_{CO} respond to reaction conditions. When P_{CO} was raised to 40 Torr, A_{CO} reached about 1/10 of its maximum value in our system: $\theta_{CO} \approx 0.06$ ML. Even under these conditions, A_{NO} remains constant near its maximum value (Fig. 11, closed squares) so θ_{CO} cannot be above 0.25 ML. (Recall that NO and CO displace one another and that A_{NO} is insensitive to changes in θ_{NO} between 0.5 and 0.75 ML). Thus, the IR data for adsorbed CO are in agreement with our previous understanding that θ_{CO} is low if $P_{NO} > 1$ Torr and $T <$ 700 K.

The RAIRS data shown in Figs. 8B and 10 show that θ_{NO} remains high—as the model predicts—as T is varied (523 K $\leq T \leq$ 673 K) with $P_{NO} = 8$ Torr. Over most of the temperature range (548 K $\leq T \leq$ 648 K, Fig. 10), A_{NO} is stable at the highest value we observed under any conditions. However, as shown in Fig. 10, A_{NO} decreases at both the lowest and highest temperatures that we examined. At low T, since θ_{CO} is low and constant (Fig. 10), it is unlikely that θ_{NO} decreases as the temperature is lowered. A more plausible explanation is that under reaction conditions (but not in vacuum) A_{NO} decreases with increasing θ_{NO} in this range because of a structural change in the adsorbate layer. At high T, it is plausible that θ_{NO} decreases as the NO adsorption-desorption equilibrium shifts more towards desorption. As the kinetic date of Fig. 4 show (closed symbols), this is exactly the temperature range (T > 673 K) where S_{N_2O} becomes T dependent; thus we expect θ_{NO} to begin to drop with increasing T in this range. Given the relatively wide range of T examined in Fig. 10, A_{NO} (and by extension θ_{NO}) remains remarkably stable. In particular, the NO desorption rate is ~4000 times faster at 700 K than at 500 K ($E_a \sim 29$ kcal/mol). The temperature-dependent data of Figs. 8B and 10 are consistent with the reaction model in Section I.

The temperature dependence discussed above is not the most rigorous test of the kinetic model—inaccurate coverages can be compensated by small changes (on the order of 2 kcal/mol) in E_a of the product generating steps. More convincing, from the RAIRS data in Figs. 11 and 12, are the effects of P_{NO} and P_{CO} on θ_{NO}. As P_{CO} increases from 1.5 to 40 Torr, Fig. 11 shows that A_{NO} falls by at most 20% so $\theta_{NO} \approx 0.5$ ML for the entire range of P_{CO}. This result is consistent both with the model and with the zero order dependence on P_{CO} of the product formation rates in Fig. 5B.

In our IR data, the only questionable agreement between model and experiment is the P_{NO} dependence. As Fig. 12 shows, with P_{CO} fixed at either 4 of 8 Torr, A_{NO} begins to decrease at $P_{NO} \approx 2$ Torr; however, given the uncertainty in A_{NO} (especially at low NO pressure and coverage), the breakpoint in Fig. 6 could occur at P_{NO} anywhere between 1 and 5 Torr. In constrast, the kinetic data of Fig. 6 clearly show that the N_2O formation rate does not fall until $P_{NO} < 1$ Torr. It is not possible with these data to unambiguously determine the breakpoint in the θ_{NO} versus P_{NO} relationship; however, the trend in the IR data is qualitatively correct: θ_{NO} falls in the same pressure regime that N_2O formation declines. This comparison between the IR and kinetic data is important because N_2O formation, which we take to be first order in θ_{NO} should fall linearly with θ_{NO} provided θ_N is constant. We assume θ_N is constant because the N_2 formation rate does not change as P_{NO} is lowered.

In summary, the IR data at high NO pressures are explained by the model discussed in Section I. The data show that for a wide range of reaction conditions with $P_{NO} > 1$ Torr and $T <$ 675 K, θ_{NO} is near saturation, and $\theta_{CO} < 0.1$ ML. Under these conditions, N_2O is the primary N containing product, the selectivity for N_2O is temperature independent, and the kinetics are zero order in both P_{NO} and P_{CO}. These observations fit well with our previous understanding that it is the stability of θ_N, θ_{NO}, and θ_{CO} that causes the reaction kinetics to be insensitive to reaction conditions.

We next consider the data with $P_{NO} < 1$ Torr. This is a different kinetic regime. The kinetic data show that the reaction orders in both NO (Fig. 6) and CO (Fig. 5) change from the zero order kinetics with $P_{NO} > 1$ Torr to positive order in NO and negative order in CO when $P_{NO} < 1$ Torr and $P_{CO} \geq 4$ Torr. The data in Fig. 3 also show that the T dependence is different with $P_{NO} < 1$ Torr. The break occurs because the selectivity for N_2O begins to decrease sharply above 575 K when we are reacting 0.8 Torr of NO (Fig. 4). At 8 Torr of NO, a similar drop in N_2O selectivity occurs at about 100 K higher (Fig. 4). The IR data give insight into the cause. At the higher P_{NO}, θ_{CO} (Figs. 9B and 10) remains low and θ_{NO} (Fig. 8B and 10) remains high between 523

and 673 K. Interestingly, exactly the opposite behavior is observed with 0.8 Torr NO. As T is raised, θ_{NO} (Figs. 8A and 10) falls linearly with $1/T$ above 548 K. Once θ_{NO} has fallen substantially, E_a for N_2O formation goes to zero. At this same temperature, the N_2 formation rate sharply increases (Fig. 3). The model in Section I explains this as follows: N_2O formation shows an $E_a \approx 0$ because this reaction is losing out to a competing reaction, NO desorption. As desorption wins out θ_{NO} drops dramatically. (We estimate that the break in the Arrhenius plot would occur around 623 K, if E_a for the NO + N elementary step is approximately 33 kcal/mol, by assuming θ_N is constant below 623 K at 0.25 ML while θ_{NO} falls linearly with $1/T$.) N_2 formation rates rise sharply at 623 K as a result of an increase in θ_N. The increase in θ_N occurs because as θ_{NO} falls, the primary process for N removal, N_2O formation, is declining rapidly.

Above, we have offered an explanation based on the temperature-dependent data. The pressure-dependent data in Fig. 12 also show that θ_{NO} is a strong function of P_{NO}. As P_{NO} is increased from 0.4 to 2 Torr, with P_{CO} fixed at either 4 or 8 Torr, A_{NO} increases linearly from our detection limit (at ~0.05 ML) to the maximum A_{NO} detected under reaction conditions (at 0.5 ML). Given the uncertainty in measured A_{NO} (especially at low P_{NO}), the breakpoint in Fig. 12 could occur anywhere between 1 and 5 Torr of NO. Comparison of Fig. 12 to the kinetic data of Fig. 6 shows that the N_2O formation rate (which we take to be first order in θ_{NO}) increases with first order kinetics up to $P_{NO} = 1$ Torr, then goes to zero order in roughly the same pressure range in which θ_{NO} stops increasing. Although there is some uncertainty in this correlation near the breakpoint in the θ_{NO} versus P_{NO} relationship, the trend in the IR data is qualitatively correct. Where θ_{NO} increases is in the same pressure range that the N_2O formation rate increases. Thus the data support our model which predicts a first order dependence of N_2O formation on θ_{NO}. This conclusion assumes that θ_N is constant, based on the kinetic data which show N_2 formation does not change as P_{NO} is changed. Similarly good qualitative agreement between θ_{NO} and N_2O formation rates were found when P_{CO} was varied (Figs. 5 and 11). Reaction rates start to fall off with roughly the same order as the IR intensities once P_{CO} is above 3–5 Torr (with P_{NO} fixed at 0.8 Torr). In summary, over a wide range of pressure and temperature, our IR data are consistent with the model discussed in Section I. The N_2O formation rate appears to be first order in θ_{NO} and in θ_N. Further, we have mapped out the pressure dependence in sufficient detail to show that θ_{NO} controls the transformation into and out of the type of zero order kinetics where the selectivity is temperature independent.

4.3. Other Possible Explanations

In Section 4.2 we showed that our IR data are explained by the model in Section I. In this model, N_2 is formed by the reaction of N + N and N_2O is formed by the reaction of NO + N. At higher temperatures and/or lower NO pressures the $NO + N \rightarrow N_2O$ reaction loses out to a competing reaction, NO desorption. It is this competition between the NO + N reaction and NO desorption which controls the selectivity of the reaction for N_2O.

An alternative mechanism is that N_2O and N_2 are formed by a common N_2O intermediate (10, 44). Steps [5] and [6] of the model in Section I are replaced with

$$NO_{(ad)} + N_{(ad)} \Rightarrow N_2O_{(a)} + S, \quad [11]$$

$$N_2O_{(a)} \Leftrightarrow N_2O_{(g)} + S, \quad [12]$$

$$N_2O_{(a)} + S \Rightarrow N_{2(g)} + O_{(a)}. \quad [13]$$

Can our IR data be explained with this mechanism? The experiment shown in Fig. 7 was performed to test the idea that product $N_2O_{(g)}$ could readsorb (step [12]) and then form N_2. By adding labeled $^{15}N_2O_{(g)}$ to the $^{14}NO_{(g)}$ and $^{12}CO_{(g)}$ reactant mixture we showed that $^{15}N_2O_{(g)}$ is not consumed during the reaction. Therefore, under the conditions studied here (648 K and low conversion) readsorption of product N_2O is not an important path to produce N_2. We have previously shown (4) that N_2O is readily converted to N_2 at $T > 700$ K.

As we understand the common intermediate model, the selectivity of the reaction is determined by the relative rates of steps [12] and [13]. Experimental data suggest that the relative rates of steps [12] and [13] depend more strongly on θ_{NO} and θ_{CO} than on differences in E_a for these two steps. This conclusion is based on data (10, 14) which show (as we did in Fig. 4) that the *temperature* at which $N_{2(g)}$ formation, step [13], dominates over $N_2O_{(g)}$ formation, step [12], is dependent on P_{NO}. θ_{NO} and θ_{CO} control the relative rates of steps [12], $N_2O_{(a)}$ desorption, and [13], $N_2O_{(a)}$ disproportionation, by limiting θ_ν for the dissociation reaction. This model is best tested by the NO pressure-dependent data of Figs. 6 and 12. The data of Fig. 12 show that as P_{NO} is increased, θ_{NO} increases and θ_{CO} decreases. In separate experiments using $CO/NO/O_2$ mixtures we found that θ_v is roughly constant during these changes in θ_{CO} and θ_{NO}. This conclusion is based on the observation that dissociative sticking of gas phase O_2 is not affected by changing P_{NO}. With constant θ_v the relative rates of N_2 and N_2O formation should be constant because the sites available for $N_2O_{(a)}$ dissociation are not changing. As Fig. 6 shows, N_2 formation remains constant as θ_{NO} and the N_2O formation rate increase. This suggests that the common intermediate mechanism connot fully explain our IR data; however, we caution that the rate for step [13] is not known. Our data are consistent with this mechanism if it is assumed that CO and NO have different tendencies to inhibit $N_2O_{(a)}$ dissociation. A better test of both proposed mechanisms would be to accurately measure the rate expressions for steps [3], [5],

and [13]. However, it is clear that the common intermediate interpretation is not essential to explain the available data. Further, the two-path mechanism is a simpler way to explain both the IR and kinetic observations. This conclusion is based primarily on the fact that the rate for $N + N \Rightarrow N_2$ is known (5) and fits well with the observed N_2 formation rates under reaction conditions, whereas the rate for the $N_2O_{(a)} + S \Rightarrow N_{2(g)} + O_{(a)}$ reaction is unknown.

V. CONCLUSIONS

We have used IR to observe surface NO and CO during the reaction of NO with CO over a Rh(111) catalyst with $0.4 \leq P_{NO} \leq 32$ Torr, $525 \leq T < 675$ K, and $0.8 \leq P_{CO} \leq 32$ Torr. Our IR data have been compared with previous kinetic data to show that surface NO coverage plays a key role in determining the activity and selectivity of the catalyst. When $P_{NO} > 1$ Torr and $T \leq 675$ K, θ_{NO} is for the most part >0.5 ML and independent of the reaction conditions. This leads to reaction kinetics which are zero order in reactant pressures and selectivities that are insensitive to reaction temperatures. When $P_{NO} < 1$ Torr then θ_{NO} falls in response to decreased P_{NO} or increased P_{CO} and T. Under these lower pressure conditions, the change of θ_{NO} leads to nonzero order kinetics and selectivities that are temperature sensitive. These combined IR and kinetic data are readily interpretable in terms of a reaction mechanism that has N_2O and N_2 formed by parallel pathways as described in Section I.

The IR spectra obtained under reaction conditions show that the CO occupies atop sites. We have also obtained IR spectra of NO on Rh(111) both under reaction conditions and in vacuum. The data of A_{NO} versus θ_{NO} in vacuum were used to infer θ_{NO} from A_{NO} data obtained under reaction conditions. In addition, the linear dependence of A_{NO} on θ_{NO} up to 0.5 ML was used to determine α_v for bridging NO on RH(111) : 0.20 ± 0.020 Å^3. This is nearly as large as α_v for CO on Cu(100) and Ru(100).

APPENDIX: ASSIGNMENT OF IR PEAKS

To our knowledge this is the first IR study of CO or NO on Rh(111) either in vacuum or under reaction conditions. Spectra of adsorbed CO during the reaction are shown in Fig. 9. We only see one peak that continuously tunes from about 2030 to 2045 cm^{-1} with increasing θ_{CO}. In vacuum, with higher θ_{CO}, we see two CO peaks. At saturation these are at 1890 and 2090 cm^{-1}, respectively. The CO peaks that we see with IR agree with previous EELS studies of CO on Rh(111) by Dubois and Somorjai (45), and Crowell and Somorjai (46). Previous vibrational studies of CO on transition metal surfaces indicate that the mode that tunes from 2030 to 2090 cm^{-1} is from atop bonded CO. The mode that tunes to 1890 cm^{-1} at saturation is from bridging CO. The existence of atop and bridging CO on Rh(111) at $\theta_{CO} = 0.75$ ML has been established by a dynamic LEED analysis (42, 43).

Electrochemical experiments have also obtained IR spectra of CO on Rh(111) (37, 47–49). In these, the C–O stretch vibrational frequency (ν_{CO}) varies as a function of electrode potential Φ at 30 and 47 cm^{-1}/V for atop and bridge CO, respectively. The variation of ν_{CO} with Φ is explained (50) both as the effect of the electrostatic field in the double layer (the vibrational Stark effect) and in terms of varying occupation of CO's anti-bonding $2\pi^*$ orbital. The range of Φ accessible in the electrochemical experiments does not include the vacuum potential of Rh(111), but when extrapolated, ν_{CO} for atop and bridge CO agree to within 20 cm^{-1} between the vacuum and electrochemical experiments. The electrochemical experiments also see an additional IR peak from CO, intermediate between ν_{CO} of atop and bridge CO, that has not been assigned.

With EELS in vacuum, it has also been shown that ν_{CO} of CO on Rh(111) is affected by coadsorbates. With 0.25 ML of K (46), ν_{CO} of atop and bridge CO are reduced to 2000 and 1710 cm^{-1}, respectively. This effect is explained as electron transfer from the K through the substrate to CO's antibonding $2\pi^*$ orbital. Similar changes in ν_{CO} are seen for other electron donors such as Na, benzene, fluorobenzene, acetylene, propylidyne, and ethylidyne (51, 52). Frequently the coadsorbates also cause to CO to switch to the three fold hollow adsorption site a high coverage. Coadsorbed CO and water on RH(111) has been studied by Wagner *et al.* (53).

The IR spectra of No on Rh(111) are more complicated than those for CO. Under reaction conditions, as shown in Fig. 8, adsorbed NO produces a broad IR band that in some circumstances extends from 1500 to 1700 cm^{-1}. This band has a main peak that shifts continuously from 1625 to 1640 cm^{-1} with increasing θ_{NO}. Under some conditions two other peaks, one below the main peak and one above it, are also seen. With NO on Rh(111) in vacuum, as shown in Fig. 13, IR shows five resolved peaks in this range. As θ_{NO} increases, intensity is gradually transferred from lower ν bands to higher ν bands. In vacuum, for θ_{NO} near saturation, we also see an NO band at 1840 cm^{-1}.

Early assignments of the vibrational modes of NO on surfaces were based on the close similarity between the molecular orbital descriptions of donor–acceptor bonding of CO and NO to a transition metal surface (54, 55). The lowest unoccupied molecular orbital of free CO is an antibonding π^* orbital. Free NO has the same electronic structure except that this orbital has one electron. Consequently, NO can either donate from or accept into this antibonding orbital while CO can only accept into it. Free $N^{14}O^{16}$ has $\nu_{NO} = 1876$ cm^{-1} (56) while free NO^+ and NO^- have $\nu_{NO} = 2343$ and 1347 cm^{-1} (57, 58), respectively. For metal nitrosyl complexes there is a correlation between ν_{NO} and both the charge on the NO (59, 60) and the energy of the

N(1s) peak in the XPS spectrum (61). Consequently, for NO on supported catalysts, the IR peaks are customarily labeled as $NO^{\delta-}$, NO, or $NO^{\delta+}$ on the basis of ν_{NO}. For example, in their study of NO on Rh/SiO_2 catalysts, Hecker and Bell (11) labeled a band with ν_{NO} in the range 1630 to 1690 cm^{-1} as $NO^{\delta-}$, a band at 1830 cm^{-1} as neutral NO, and a band at 1910 cm^{-1} as $NO^{\delta+}$. The vibrational frequency of even neutral NO is affected by local electrostatic field. The calculated effect for free NO oriented in the field direction (25) is 28 cm^{-1}/(V/Å). An *ab initio* calculation of a similar effect for NO^- on Ag(111) has been reported by Bagus and Illas (62).

The assignment of these modes to specific adsorption sites on the basis of ν_{NO} alone is difficult since NO at a single site on a transition metal surface has been observed to have multiple vibrational frequencies. For example, both IR (63) and EELS experiments (64) with NO on Ni(111) saw a mode in the 1460 to 1581 cm^{-1} range that was originally attributed to bridging NO. However, it has subsequenltly been shown that this NO species is at threefold hollow sites (65–69). A similar lack of correlation between NO bonding geometry and ν_{NO} has also been noted for metal nitrosyl complexes (70).

Vibrational spectra of NO on Rh(111) in vacuum have previously been obtained with EELS by Root *et al.* (71, 72) and by Kao *et al.* (24). In contrast to the multiple peaks that we observe in the 1500 to 1700 cm^{-1} range, the EELS experiments saw a single peak that tuned continuously from 1480 to 1630 cm^{-1} with increasing θ_{NO}. Root *et al.* also saw a NO peak at 1840 cm^{-1} at saturation θ_{NO}, and Kao *et al.* (24) were able to prepare a c (2×2) ordered overlayer with peaks at 1840 and 1515 cm^{-1}. Our observation of multiple NO vibrational peaks in the 1500 to 1700 cm^{-1} range with IR, while EELS saw only one, is explained by the lower resolution of EELS. A similar difference was reported for NO on Ni(111). With IR, Erley (63) saw a peak at 1460 cm^{-1} at low θ_{NO} and a peak at 1581 cm^{-1} at saturation coverage. At intermediate θ_{NO}, there were two peaks separated by 30 cm^{-1}. The low θ_{NO} peak continuously tuned into the lower of these; the high θ_{NO} peak continuously evolved from the upper of these. As θ_{NO} increased, IR intensity was continuously transferred from the lower ν_{NO} peak to the upper ν_{NO} peak. In contrast, an EELS study (64) of NO on Ni(111) saw only one peak that continuously tuned from low θ_{NO} to high θ_{NO}.

For (2×2) NO on Rh(111), a dynamic LEED analysis concluded that both atop and twofold bridge sites are occupied (24). On this basis the 1515 and 1830 cm^{-1} modes were assigned to twofold bridging and atop bonded NO, respectively. This assignment was recently questioned by Borg *et al.* (73) which led us to re-examine the HREELS assignments for the c(2×2) NO–Rh(111) surface. Using scanned angle X-ray photoelectron diffraction (XPD) in conjunction with single scattering cluster theory and R-factor analysis, we determined that the 1515 cm^{-1} mode is best explained by NO in the threefold hollow sites (74). Under reaction conditions, in our experiment, only NO with ν_{NO} from 1500 to 1700 cm^{-1} is present. Our recent XPD data (74) strongly suggests that the lowest frequency species are due to hollow site adsorption. Further, by analogy to Ni(111) (65–69), we would expect that all species below 1600 cm^{-1} are in hollow sites. As for the species between 1600 and 1700 cm^{-1}, no structural data are available. It is plausible that the peaks in the 1600 to 1700 cm^{-1} range are from threefold hollow site adsorption with differing neighboring species. When NO is coadsorbed with ethylidyne on Rh(111) (75) the NO occupies threefold hollow sites and has $\nu_{NO} = 1435$ cm^{-1}.

In summary, in vacuum, at θ_{CO} near saturation, CO occupies both atop and twofold bridge sites. In vacuum, at high θ_{NO} the NO occupies both atop and threefold hollow sites. Under reaction conditions, only atop CO and bridging (either twofold or threefold) NO are seen on Rh(111). The most plausible explanation of the multiple NO peaks in the IR spectrum (1500 to 1700 cm^{-1}) is from hollow site (threefold) NO in different local environments. However, we do not exclude the possibility that the higher frequency ($\sim$1700 cm^{-1}) modes are due to twofold bridging NO.

ACKNOWLEDGMENTS

H. Permana acknowledges financial support from the National Science Foundation [CTS-9510697] and from General Motors.

REFERENCES

1. Taylor, K. C., *Catal. Rev.-Sci. Eng.* **35**, 457 (1993).
2. Calvert, J. G., Heywood, J. B., Sawyer, R. F., and Seinfeld, J. H., *Science* **261**, 37 (1993).
3. Permana, H., Ng, K. Y. S., Peden, C. H. F., Schmieg, S. J., and Belton, D. N., *J. Phys. Chem.* **99**, 16344 (1995).
4. Belton, D. N., and Schmieg, S. J., *J. Catal.* **144**, 9 (1993); *J. Catal.* **138**, 70 (1992).
5. Belton, D. N., DiMaggio, C. L., and Ng, K. Y. S., *J. Catal.* **144**, 273 (1993).
6. Ng, K. Y. S., Belton, D. N., Schmieg, S. J., and Fisher, G. B., *J. Catal.* **146**, 394 (1994).
7. Peden, C. H. F., Belton, D. N., and Schmieg, S. J., *J. Catal.* **155**, 204 (1995).
8. Hecker, W. C., and Bell, A. T., *J. Catal.* **85**, 389 (1984).
9. Oh, S. H., Fisher, G. B., Carpenter, J. E., and Goodman, D. W., *J. Catal.* **100**, 360 (1986).
10. Cho, B. K., *J. Catal.* **138**, 255 (1992).
11. Hecker, W. C., and Bell, A. T., *J. Catal.* **84**, 200 (1983).
12. Chin, A. A., and Bell, A.T., *J. Phys. Chem.* **87**, 3700 (1983).
13. Cho, B. K., Shanks, B. H., and Bailey, J. E., *J. Catal.* **115**, 486 (1989).
14. Cho, B. K., *J. Catal.* **131**, 74 (1991).
15. Peden, C. H. F., Goodman, D. W., Blair, D. S., Berlowitz, P. J., Fisher, G. B., and Oh, S. H., *J. Phys. Chem.* **92**, 1563 (1988).
16. Schwartz, S. B., Fisher, G. B., and Schmidt, L. D., *J. Phys. Chem.* **92**, 389 (1988).
17. Fisher, G. B., and Schmieg, S. J., *J. Vac. Sci. Technol. A* **1**, 1064 (1983).
18. Bolotin, G. A., and Chukina, T. P., *Opt. Spektrosk.* **23**, 620 (1967) [*Opt. Spectrosc. (USSR)* **23**, 333 (1967)].

19. Weaver, J. H., Krafka, C., Lynch, D. W., and Koch, E. E., "Physics Data, Optical Properties of Metals, Part I: The Transition Metals," p. 174. Fachinformationszentrum, Karlsruhe, Germany, 1981.
20. Lambert, D. K., *J. Chem. Phys.* **89**, 3847 (1988).
21. Tobin, R. G., *Phys. Rev. B* **45**, 12110 (1992).
22. Chabal, Y. J., *Surf. Sci. Rep.* **8**, 211 (1988).
23. Goodman, D. W., private communication.
24. Kao, C.-T., Blackman, G. S., Van Hove, M. A., Somorjai, G. A., and Chan, C.-M, *Surf. Sci.* **224**, 77 (1989).
25. Lambert, D. K., *Solid State Commun.* **51**, 297 (1984).
26. Persson, B. N. J., and Ryberg, R., *Phys. Rev. B* **24**, 6954 (1981).
27. Schweizer, E., Persson, B. N. J., Tüshaus, M., Hoge, D., and Bradshaw, A. M., *Surf. Sci.* **213**, 49 (1989).
28. Xu, X., Chen, P., and Goodman, D. W., *J. Phys. Chem.* **98**, 9242 (1994).
29. Vesecky, S. M., Chen, P., Xu, X., and Goodman, D. W., *J. Vac. Sci. Technol. A* **13**, 1539 (1995).
30. Dumas, P., Tobin, R. G., and Richards, P. L., *Surf. Sci.* **171**, 579 (1986).
31. Hermann, K., Bagus, P. S., and Bauschlicher, C. W. Jr., *Phys. Rev. B* **30**, 7313 (1984).
32. Hollins, P., and Pritchard, J., *in* "Vibrational Spectroscopy of Adsorbates" (R.F. Willis, Ed.), p. 125. Springer, Berlin, 1980.
33. Borguet, E., and Dai, H. L., *J. Chem. Phys.* **101**, 9080 (1994).
34. Pfnür, H., Menzel, D., Hoffmann, F. M., Ortega, A., and Bradshaw, A. M., *Surf. Sci.* **93**, 431 (1980).
35. Ortega, A., Haffmann, F. M., and Bradshaw, A. M., *Surf. Sci.* **119**, 79 (1982).
36. Leung, L.-W. H., He, J. W., and Goodman, D. W., *J. Chem. Phys.* **93**, 8328 (1990).
37. Leung, L.-W. H., Chang, S.-C., and Weaver, M. J., *J. Chem. Phys.* **90**, 7426 (1989).
38. Bridge, N. J., and Buckingham, A. D., *Proc. Roy. Soc. London, Ser. A* **295**, 334 (1966).
39. Luo, J. S., Tobin, R. G., and Lambert, D. K., *Chem. Phys. Lett.* **204**, 445 (1993).
40. Wang, H., Tobin, R. G., and Lambert, D. K., *J. Chem. Phys.* **101**, 4277 (1994).
41. Wang, H., Tobin, R. G., Lambert, D. K., Fisher, G. B., and DiMaggio, C. L., *J. Chem. Phys.* **103**, 2711 (1995).
42. Van Hove, M. A., Koestner, R. J., and Somorjai, G. A., *Phys. Rev. Lett.* **50**, 903 (1983).
43. Van Hove, M. A., Koestner, R. J., Frost, J. C., and Somorjai, G. A., *Surf. Sci.* **129**, 482 (1983).
44. Cho, B. K., *J. Catal.* **148**, 697 (1994).
45. Dubois, L. H., and Somorjai, G. A., *Surf. Sci.* **91**, 514 (1980).
46. Crowell, J. E., and Somorjai, G. A., *Appl. Surf. Sci.* **19**, 73 (1984).
47. Hahn, F., Beden, B., and Lamy, C., *J. Electroanal. Chem.* **204**, 315 (1986).
48. Chang, S.-C., and Weaver, M. J., *Surf. Sci.* **238**, 142 (1990).
49. Chang, S.-C., and Weaver, M. J., *J. Phys. Chem.* **95**, 5391 (1991).
50. Lambert, D. K., *Electrochim. Acta* **41**, 623 (1996).
51. Mate, C. M., and Somorjai, G. A., *Surf. Sci.* **160**, 542 (1985).
52. Mate, C. M., Bent, B. E., and Somorjai, G. A., *J. Electron Spectrosc. Relat. Phenom.* **39**, 205 (1986).
53. Wagner, F. T., Moylan, T. E., and Schmeig, S. J., *Surf. Sci.* **195**, 403 (1988).
54. Blyholder, G., and Allen, M. C., *J. Phys. Chem.* **69**, 3998 (1965).
55. Sung, S.-S., Hoffmann, R., and Thiel, P. A., *J. Phys. Chem.* **90**, 138 (1986).
56. Johns, J. W. C., Reid, J., and Lepard, D. W., *J. Mol. Spectrosc.* **65**, 155 (1977).
57. Herzberg, G., "Spectra of Diatomic Molecules," p. 92. Van Nostrand–Reinhold, New York, 1950.
58. Huber, K. P., and Herzberg, G., "Constants of Diatomic Molecules," pp. 482, 484. Van Nostrand–Reinhold, New York, 1979.
59. Heiber, V. W., and Jahn, A., *Z. Naturforschg. B: Anorg. Chem. Org. Chem.* **13**, 195 (1958).
60. Bottomley, F., Brooks, W. V. F., Clarkson, S. G., and Tong, S.-B., *J. Chem. Soc. Chem. Commun.* **1973**, 919 (1973).
61. Finn, P., and Jolly, W. L., *Inorg. Chem.* **11**, 893 (1972).
62. Bagus, P. S., and Illas, F., *Chem. Phys. Lett.* **224**, 576 (1994).
63. Erley, W., *Surf. Sci.* **205**, L771 (1988).
64. Lehwald, S., Yates, J. T., Jr., and Ibach, H., *in* "Proceedings of the Fourth International Conference on Solid Surfaces and the Third European Conference on Surface Science" (D. A. Degras and M. Costa, Eds.), Vol. 1, p. 221. Soc. Française du Vide, Paris, 1980.
65. Aminpirooz, S., Schmalz, A., Becker, L., and Haase, J., *Phys. Rev. B* **45**, 6337 (1992).
66. Asensio, M. C., Woodruff, D. P., Robinson, A. W., Schindler, K,-M., Gardner, P., Ricken, D., Bradshaw, A. M., Conesa, J. C., and González-Elipe, A. R., *Chem. Phys. Lett.* **192**, 259 (1992).
67. Asensio, M. C., Woodruff, D. P., Robinson, A. W., Schindler, K.-M., Gardner, P., Ricken, D., Bradshaw, A. M., Conesa, J. C., and González-Elipe, A. R., *J. Vac. Sci. Technol. A* **10**, 2445 (1992).
68. Mapledoram, L. D., Wander, A., and King, D. A., *Chem. Phys. Lett.* **208**, 409 (1993).
69. Materer, N., Barbieri, A., Gardin, D., Starke, U., Batteas, J. D., Van Hove, M. A., and Somorjai, G. A., *Phys. Rev. B* **48**, 2859 (1993).
70. Enemark, J. H., and Feltham, R. D., *Coord. Chem. Rev.* **13**, 339 (1974).
71. Root, T. W., Fisher, G. B., and Schmidt, L. D., *J. Chem. Phys.* **85**, 4679 (1986).
72. Root, T. W., Fisher, G. B., and Schmidt, L. D., *J. Chem. Phys.* **85**, 4687 (1986).
73. Borg, H. J., Reijerse, J. F. C.-J. M., van Santen, R. A., and Niemantsverdriet, J. W., *J. Chem. Phys.* **101**, 10052 (1994).
74. Kim, Y. J., Herman, G. S., Thevuthasan, T., Peden, C. H. F., Chambers, S. A., Belton, D. N., and Permana, H., submitted for publication.
75. Blackman, G. S. Kao, C. T., Bent, B. E., Mate, C. M., Van Hove, M. A., and Somorjai, G. A., *Surf. Sci.* **207**, 66 (1988).